Chapter 15

Light Scattering and Radiative Transfer in Ice Crystal Clouds: Applications to Climate Research

K. N. Liou, Yoshihide Takano, and Ping Yang
Department of Atmospheric Sciences
University of California, Los Angeles
Los Angeles, California 90095

Light Scattering by Nonspherical Particles: Theory, Measurements, and Applications

I. INTRODUCTION

Understanding the radiation budget of Earth and the atmosphere system, and hence its climate, must begin with an understanding of the scattering and absorption properties of cloud particles. A large number of cloud particles are nonspherical ice crystals. Basic scattering, absorption, and polarization data for the type of nonspherical ice crystals that occur in cirrus clouds are required for reliable modeling of their radiative properties for incorporation in climate models; for interpretation of the observed bidirectional reflectances, fluxes, and heating rates from the air, the ground, and space; and for development of remote-sensing techniques to infer cloud optical depth, temperature, and ice crystal size. Moreover, because of the limitation of our present knowledge and understanding, fundamental investigation of the light-scattering and polarization characteristics of nonspherical ice crystals is also an important scientific subject in its own right.

Laboratory experiments reveal that the shape and size of an ice crystal are governed by temperature and supersaturation, but it generally has a basic hexagonal structure. In the atmosphere, if the ice crystal growth involves collision and coalescence, its shape can be extremely complex. Recent observations based on aircraft optical probes and replicator techniques for midlatitude, tropical, and contrail cirrus show that these clouds are largely composed of bullet rosettes, solid and hollow columns, plates, aggregates, and ice crystals with irregular surfaces with sizes ranging from a few micrometers to 1000 μm. In addition to the nonspherical shape problem, a large variation of size parameters at the solar and thermal infrared wavelengths also presents a basic difficulty in light-scattering calculations.

We wish to address the issue of the variability of size parameter for nonspherical ice crystals in fundamental electromagnetic scattering and present a unified theory for light scattering by ice crystals covering all sizes and shapes that can be defined mathematically or numerically. Further, we shall illustrate the importance of the basic scattering, absorption, and polarization data for ice crystals in climate and remote-sensing research.

II. UNIFIED THEORY FOR LIGHT SCATTERING BY ICE CRYSTALS

The scattering of light by spheres can be solved by the exact Lorenz–Mie theory and computations can be performed for the size parameters that are practical for atmospheric applications. However, an exact solution for the scattering of light by nonspherical ice crystals covering all sizes and shapes that occur in Earth's atmosphere does not exist in practical terms. It is unlikely that one specific method

can be employed to resolve all the scattering problems associated with nonspherical ice crystals. In the following, we present a unified theory for light scattering by ice crystals by means of a combination of geometric optics and finite difference time domain methods.

A. Geometric Ray Tracing

The principles of geometric optics are the asymptotic approximations of the fundamental electromagnetic theory, valid for light-scattering computations involving a target whose dimension is much larger than the incident wavelength. The geometric optics method has been employed to identify the optical phenomena occurring in the atmosphere, such as halos, arcs, and rainbows. In addition, it is the only practical approach for the solutions of light scattering by large nonspherical particles at this point. In this section we shall review the conventional and improved approaches, the methodology dealing with absorption in the context of geometric ray tracing, and the numerical implementation by the Monte Carlo method. As we have published a series of papers on this subject (Liou and Coleman, 1980; Liou, 1980, 1992; Cai and Liou, 1982; Takano and Liou, 1989a, b, 1995; Liou and Takano, 1994; Yang and Liou, 1995, 1996b, 1997, 1998a), only the fundamentals and the associated equations will be presented here. References of the relevant works can be found in these papers.

1. Conventional Approach

When the size of a scatterer is much larger than the incident wavelength, a light beam can be thought of as consisting of a bundle of separate parallel rays that hit the particle. Each ray will then undergo reflection and refraction and will pursue its own path along a straight line outside and inside the scatterer with propagation directions determined by the Snell law only at the surface. In the context of geometric optics, the total field is assumed to consist of the diffracted rays and the reflected and refracted rays, as shown in Fig. 1a. The diffracted rays pass around the scatterer. The rays impinging on the scatterer undergo local reflection and refraction, referred to as Fresnelian interaction. The energy that is carried by the diffracted and the Fresnelian rays is assumed to be the same as the energy that is intercepted by the particle cross section projected along the incident direction. The intensity of the far-field scattered light within the small scattering-angle interval $\Delta\Theta$ in the scattering direction Θ can be computed from the summation of the intensity contributed by each individual ray emerging in the direction between $\Theta + \Delta\Theta/2$ and $\Theta - \Delta\Theta/2$. Except in the method presented by Cai and Liou (1982), all the conventional geometric ray-tracing techniques have not accounted for phase interferences between relevant rays. It is usually assumed that

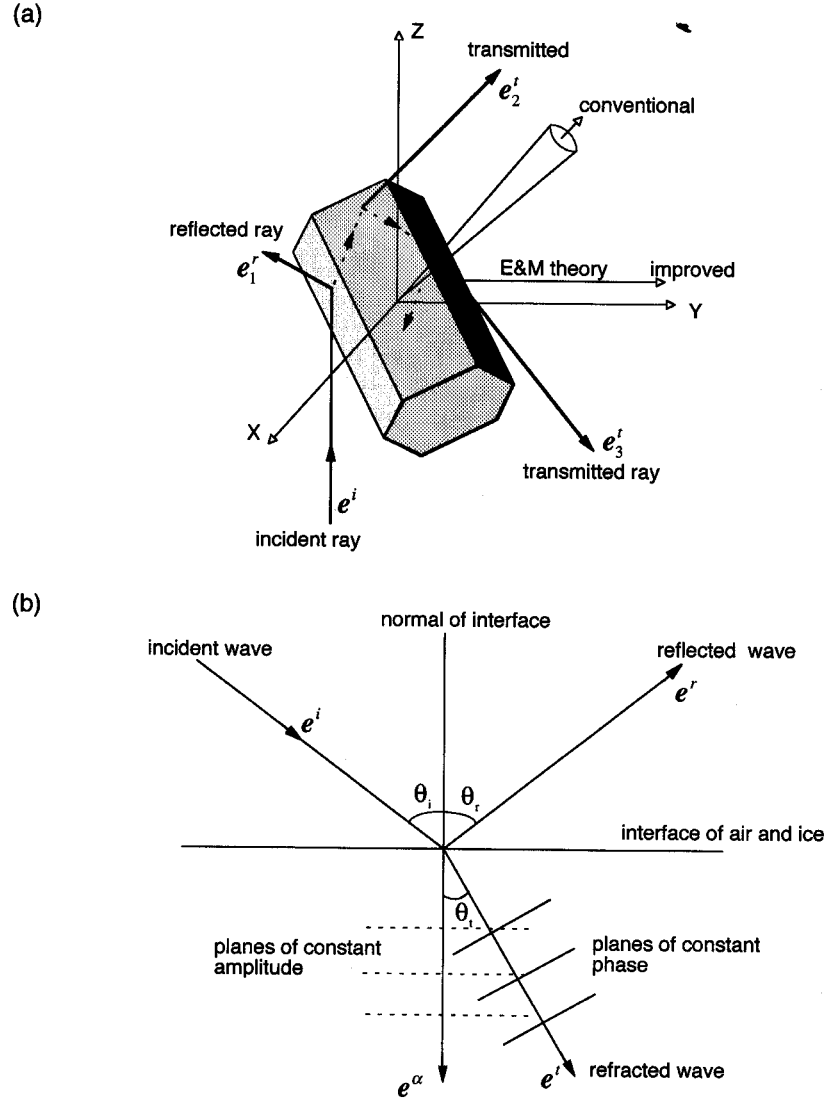

Figure 1 (a) Geometry of ray tracing involving a hexagon in three-dimensional space. Conventional and improved methods are also indicated in the diagram. (b) Geometric ray tracing in a medium with absorption. The planes of constant amplitude of the refracted wave are parallel to the interface, whereas the direction of the phase propagation for the inhomogeneous wave inside the medium is determined via Snell's law.

the interference is smoothed out when the particles are randomly oriented. In this case the extinction efficiency (the ratio of the extinction cross section to the average projected area of the particle) of the scatterer is 2. On the basis of Babinet's principle, diffraction by a scatterer may be regarded as that by an opening on an opaque screen perpendicular to the incident light, which has the same geometric shape as the projected cross section of the scatterer. The well-known Fraunhofer diffraction formula can be employed to compute the diffraction component for hexagonal ice particles.

In the geometric ray-tracing method, the directions of the rays are first determined. In reference to Fig. 1a, they can be defined by the following unit vectors:

$$\mathbf{e}_p^r = \mathbf{x}_p - 2(\mathbf{x}_p \cdot \mathbf{n}_p)\mathbf{n}_p, \qquad p = 1, 2, 3, \ldots, \tag{1a}$$

$$\mathbf{e}_p^t = \frac{1}{m_p}\left\{\mathbf{x}_p - (\mathbf{x}_p \cdot \mathbf{n}_p)\mathbf{n}_p - \left[m_p^2 - 1 + (\mathbf{x}_p \cdot \mathbf{n}_p)^2\right]^{1/2}\mathbf{n}_p\right\}, \qquad p = 1, 2, 3, \ldots, \tag{1b}$$

$$\mathbf{x}_p = \begin{cases} \mathbf{e}^i, & p = 1, \\ \mathbf{e}_1^t, & p = 2, \\ \mathbf{e}_{p-1}^r, & p \geq 3, \end{cases} \tag{1c}$$

where $m_p = m$ for $p = 1$ and $m_p = 1/m$ for $p > 1$, with m being the refractive index, and $\mathbf{n}_p$ denote the unit vectors normal to the surface. When $m_p^2 < 1 - (\mathbf{x}_p \cdot \mathbf{n}_p)^2$, total reflection occurs and there will be no refracted ray. The electric fields for two polarization components associated with the rays can be computed from the Fresnel formulas [see Eqs. (18a) and (18b)]. Summing the energies of the rays that emerge within a preset small scattering-angle interval in a given direction, the phase function can be obtained for this part. Let the normalized phase functions [i.e., (1, 1) element of the scattering matrix] for the parts of reflection and refraction and diffraction be F_{11}^r and F_{11}^d, respectively. Then the normalized phase function is $F_{11} = (1 - f_d)F_{11}^r + f_d F_{11}^d$, where $f_d = 1/2\varpi(1 - f_\delta)$ with f_δ being the delta transmission associated with 0° refraction produced by two parallel prismatic faces and ϖ being the single-scattering albedo, which can be determined from the absorption of individual rays and the constant extinction efficiency.

2. Improved Geometric Optics Approach

The laws of geometric optics are applicable to the scattering of light by a particle if its size is much larger than the incident wavelength so that geometric rays can be localized. In addition to the requirement of the localization principle, the conventional geometric ray-tracing technique assumes that the energy attenuated by the scatterer may be decomposed into equal extinction from diffraction and

Fresnel rays. Moreover, the Fraunhofer diffraction formulation used in geometric ray tracing does not account for the vector property of the electromagnetic field and requires a Kirchhoff boundary condition, which cannot take into consideration the effects of the changes along the edge contour of the opening. Finally, calculations of the far field directly by ray tracing will produce a discontinuous distribution of the scattered energy, such as the delta transmission noted by Takano and Liou (1989a).

To circumvent a number of shortcomings in the conventional geometric optics approach, an improved method has been developed (Yang and Liou, 1995, 1996b). It is simple in concept in that the energies determined from geometric ray tracing at the particle surface are collected and mapped to the far field based on the exact electromagnetic wave theory. In this manner, the only approximation is on the internal geometric ray tracing. This differs from the conventional approach, which collects energies produced by geometric reflections and refractions directly at the far field through a prescribed solid angle.

The tangential components of the electric and magnetic fields on surface S that encloses the scatterer can be used to determine the equivalent electric and magnetic currents for the computation of the scattered far field on the basis of the electromagnetic equivalence theorem (Schelkunoff, 1943). In this theorem, the electromagnetic field detected by an observer outside the surface would be the same as if the scatterer were removed and replaced by the equivalent electric and magnetic currents given by

$$\mathbf{J} = \mathbf{n}_S \times \mathbf{H}, \tag{2a}$$

$$\mathbf{M} = \mathbf{E} \times \mathbf{n}_S, \tag{2b}$$

where $\mathbf{n}_S$ is the outward unit vector normal to the surface. For the far-field region, we have

$$\mathbf{E}^s(\mathbf{r}) = \frac{\exp(ikr)}{ikr} \frac{k^2}{4\pi} \left(\frac{\mathbf{r}}{r}\right) \times \iint_S \left[\mathbf{M}(\mathbf{r}') + \left(\frac{\mathbf{r}}{r}\right) \times \mathbf{J}(\mathbf{r}')\right] \exp\left(-ik\mathbf{r} \cdot \frac{\mathbf{r}'}{r}\right) d^2\mathbf{r}', \tag{3}$$

where $\mathbf{r}/r$ denotes the scattering direction, $\mathbf{r}$ is the reference position vector, $\mathbf{r}'$ is the position vector of the source point, k is the wavenumber, and $i = \sqrt{-1}$. The far-field solution can also be determined by a volume integral involving the internal field.

By means of geometric ray tracing, the electric field on the surface of a particle can be evaluated after the successive application of Fresnel reflection and refraction coefficients parallel and perpendicular to a defined reference plane at the point of interaction taking into account the path length in the three-dimensional

geometry. If an ice crystal shape is of great complexity such as an aggregate, the surface can be defined as a cubic box so that the computation of the electric field can be conducted on a regularly shaped surface. The electric field can be defined on the illuminated and shadowed sides as follows:

$$\mathbf{E}(\mathbf{r}) = \begin{cases} \mathbf{E}_a(\mathbf{r}) + \mathbf{E}_b(\mathbf{r}), & \mathbf{r} \in \text{illuminated side}, \\ \mathbf{E}_b(\mathbf{r}), & \mathbf{r} \in \text{shadowed side}, \end{cases} \tag{4a}$$

where

$$\mathbf{E}_a(\mathbf{r}) = \mathbf{E}_i(\mathbf{r}) + \mathbf{E}_1^r(\mathbf{r}), \tag{4b}$$

$$\mathbf{E}_b(\mathbf{r}) = \sum_{p=2}^{\infty} \mathbf{E}_p^t(\mathbf{r}). \tag{4c}$$

In these equations, $\mathbf{E}_i$ is the incident electric field, $\mathbf{E}_1^r$ is the electric field for external reflection, and $\mathbf{E}_p^t$ are the electric fields produced by two refractions and internal reflections ($p \geq 2$). Because the transverse electromagnetic wave condition is implied in ray tracing, the magnetic field for each reflection and refraction can be obtained from

$$\mathbf{H}_p^{r,t}(\mathbf{r}) = \mathbf{e}_p^{r,t} \times \mathbf{E}_p^{r,t}(\mathbf{r}) \qquad \text{for } \mathbf{r} \in \text{ outside the particle.} \tag{5}$$

In practice, the mapping of the near-field solution to the far field can be done in its entirety for $\mathbf{E}_a$ in Eq. (4b). But for $\mathbf{E}_b$ in Eq. (4c), the mapping is done ray by ray and the results will include the diffraction pattern. Full account of phase interferences is taken in this mapping process in the determination of the phase function.

In accord with the conservation principle for electromagnetic energy concerning the Poynting vector (Jackson, 1975), the extinction and absorption cross sections of the particle can be derived as follows:

$$C_{\text{ext}} = \text{Im}\left\{ \frac{k}{|\mathbf{E}_i|^2}(\varepsilon - 1) \iiint_V \mathbf{E}(\mathbf{r}') \cdot \mathbf{E}_i^*(\mathbf{r}')\, d^3\mathbf{r}' \right\}, \tag{6a}$$

$$C_{\text{abs}} = \frac{k}{|\mathbf{E}_i|^2}\varepsilon_i \iiint_V \mathbf{E}(\mathbf{r}') \cdot \mathbf{E}^*(\mathbf{r}')\, d^3\mathbf{r}', \tag{6b}$$

where the asterisk denotes the complex conjugate, ε_i is the imaginary part of the permittivity, and V is the particle volume.

Finally, when the ray-tracing technique is applied to obtain the surface field, one must properly account for the area elements from which the externally reflected and transmitted localized waves make a contribution to the surface field. If the cross section of the incident localized wave is $\Delta\sigma_i$, the area on the particle

surface for external reflection is

$$\Delta\sigma_1^r = -\Delta\sigma_i(\mathbf{n}_i \cdot \mathbf{e}^i)^{-1}. \tag{7a}$$

For the transmitted rays, the area is given by

$$\Delta\sigma_p^t = -\Delta\sigma_i(\mathbf{n}_1 \cdot \mathbf{e}_1^t)\left[(\mathbf{n}_1 \cdot \mathbf{e}^i)(\mathbf{n}_p \cdot \mathbf{e}_p^t)\right]^{-1}, \qquad p = 2, 3, 4, \ldots, \tag{7b}$$

where all unit vectors have been defined in Eqs. (1a)–(1c). The radius of the cross section of a ray should be on the order of k^{-1} so that the phase change over the ray cross section is not significant and permits proper account of the phase interference of the localized waves by using the phase information at the centers of the rays. Because the phase variation over the ray cross section can be neglected, the numerical results are not sensitive to the shape of the ray cross sections. We may use a circular shape in the calculations.

3. Absorption Effects in Geometric Optics

The geometric optics approach that has been used in the past generally assumes that the effect of absorption within the particle on the propagating direction of a ray can be neglected so that the refracted angle and the ray path length can be computed from Snell's law and the geometry of the particle. This is a correct approach if absorption is weak, such as that of ice and water at most solar wavelengths. For strong absorption cases, rays refracted inside the particle are almost totally absorbed so that the geometric optics method can also be used to compute diffraction and external reflection as long as the particle size is much larger than the incident wavelength. Although the preceding argument is physically correct in the limits of weak and strong absorption, we shall consider the general absorption effect in the context of geometric optics based on the fundamental electromagnetic wave theory. Note that the effect of the complex refractive index on geometric optics has been formulated only for the Fresnel coefficients (Stratton, 1941; Born and Wolf, 1970).

Consider the propagation of the incident wave from air into ice (Fig. 1b). The wave vectors associated with the incident and reflected waves are real because these waves, which are outside the ice medium, must have the same properties. However, the wave vector of the refracted wave is complex; this is referred to as the inhomogeneity effect. These wave vectors can be represented by

$$\mathbf{k}_i = k\mathbf{e}^i, \qquad \mathbf{k}_r = k\mathbf{e}^r, \qquad \mathbf{k}_t = k_t\mathbf{e}^t + ik_\alpha\mathbf{e}^\alpha, \tag{8}$$

where $\mathbf{e}^i$, $\mathbf{e}^r$, $\mathbf{e}^t$, and $\mathbf{e}^\alpha$ are unit vectors; the subscripts i, r, and t denote the incident, reflected, and refracted waves, respectively; $k = 2\pi/\lambda$ in which λ is the wavelength in air; and k_t and k_α are two real parameters that determine the

complex wave vector of the refracted wave. For nonabsorptive cases, k_α is zero. The corresponding electric vectors can be expressed by

$$\mathbf{E}_i(\mathbf{r}, t) = \mathbf{A}_i \exp\left[i(k\mathbf{r} \cdot \mathbf{e}^i - \omega t)\right], \tag{9a}$$

$$\mathbf{E}_r(\mathbf{r}, t) = \mathbf{A}_r \exp\left[i(k\mathbf{r} \cdot \mathbf{e}^r - \omega t)\right], \tag{9b}$$

$$\mathbf{E}_t(\mathbf{r}, t) = \mathbf{A}_t \exp\left[i(k_t\mathbf{r} \cdot \mathbf{e}^t + ik_\alpha \mathbf{e}^\alpha - \omega t)\right], \tag{9c}$$

where $\mathbf{A}_i$, $\mathbf{A}_r$, and $\mathbf{A}_t$ are the amplitudes and ω is the circular frequency. Further, we define the following parameters:

$$N_\mathrm{r} = \frac{k_t}{k}, \qquad \tilde{N}_\mathrm{i} = \frac{k_\alpha}{k}. \tag{10}$$

At the interface of the two media, at which the position vector is denoted as $\mathbf{r}_S$, the phases of the wave vibration must be the same for the incident, reflected, and refracted waves. Thus from Eqs. (8) and (10) we obtain

$$\mathbf{e}^i \cdot \mathbf{r}_S = \mathbf{e}^r \cdot \mathbf{r}_S = N_\mathrm{r}(\mathbf{e}^t \cdot \mathbf{r}_S) + i\tilde{N}_\mathrm{i}(\mathbf{e}^\alpha \cdot \mathbf{r}_S). \tag{11}$$

Because the wave vectors for the incident and reflected waves are real, we must have

$$\mathbf{e}^i \cdot \mathbf{r}_S = \mathbf{e}^r \cdot \mathbf{r}_S = N_\mathrm{r}(\mathbf{e}^t \cdot \mathbf{r}_S), \qquad \mathbf{e}^\alpha \cdot \mathbf{r}_S = 0. \tag{12}$$

Based on the geometry defined by Eq. (12), a generalized form of the Snell law can be derived and is given by

$$\sin\theta_i = \sin\theta_r, \qquad \sin\theta_t = \frac{\sin\theta_i}{N_\mathrm{r}}, \tag{13}$$

where θ_i, θ_r, and θ_t denote the incident, reflected, and refracted angles, respectively (Fig. 1b). The vector $\mathbf{e}_\alpha$ in Eq. (12) is normal to the interface of the two media. It follows that the planes of constant amplitude of the refracted wave are parallel to the interface. To determine N_r and N_i, we use the electric field of the refracted wave, which must satisfy the wave equation in the form

$$\nabla^2\mathbf{E}_t(\mathbf{r}, t) - \frac{(m_\mathrm{r} + im_\mathrm{i})^2}{c^2}\frac{\partial^2\mathbf{E}_t(\mathbf{r}, t)}{\partial t^2} = 0, \tag{14}$$

where c is the speed of light in vacuum and m_r and m_i are the real and imaginary parts of the refractive index, respectively. Substituting Eq. (9c) into Eq. (14) and using Eq. (10) lead to

$$N_\mathrm{r}^2 - \tilde{N}_\mathrm{i}^2 = m_\mathrm{r}^2 - m_\mathrm{i}^2, \qquad N_\mathrm{r}\tilde{N}_\mathrm{i}\cos\theta_t = m_\mathrm{r}m_\mathrm{i}. \tag{15}$$

Let $N_i = \tilde{N}_i \cos\theta_t$. Then from Eqs. (12) and (15), we obtain

$$N_r = \frac{\sqrt{2}}{2}\left\{m_r^2 - m_i^2 + \sin^2\theta_i + \left[\left(m_r^2 - m_i^2 - \sin^2\theta_i\right)^2 + 4m_r^2 m_i^2\right]^{1/2}\right\}^{1/2}, \tag{16a}$$

$$N_i = \frac{m_r m_i}{N_r}. \tag{16b}$$

These two parameters are referred to as the adjusted real and imaginary refractive indices.

After determining N_r and N_i, the refracted wave given in Eq. (9c) can be rewritten in the form

$$\mathbf{E}_t(\mathbf{r}, t) = \mathbf{A}_t \exp(-kN_i l_a) \exp\left[i(kN_r \mathbf{e}^t \cdot \mathbf{r} - \omega t)\right], \tag{17}$$

where $l_a = (\mathbf{e}^\alpha \cdot \mathbf{r})/\cos\theta_t$ is the distance of the propagation of the refracted wave along the direction $\mathbf{e}^t$. It is clear that the direction of the phase propagation for the inhomogeneous wave inside the medium is determined by N_r via Snell's law, whereas the attenuation of the wave amplitude during the wave propagation is determined by N_i. Consequently, the refracted wave can be traced precisely. Following Yang and Liou (1995), the Fresnel reflection and refraction coefficients in terms of the adjusted real and imaginary refractive indices are given by

$$R_l = \frac{N_r \cos\theta_i - \cos\theta_t}{N_r \cos\theta_i + \cos\theta_t}, \qquad T_l = \frac{2\cos\theta_i}{N_r \cos\theta_i + \cos\theta_t}, \tag{18a}$$

$$R_r = \frac{\cos\theta_i - N_r \cos\theta_t}{\cos\theta_i + N_r \cos\theta_t}, \qquad T_r = \frac{2\cos\theta_i}{\cos\theta_i + N_r \cos\theta_t}, \tag{18b}$$

where the subscripts l and r denote the horizontally and vertically polarized components, respectively.

4. Monte Carlo Method for Ray Tracing

Use of the Monte Carlo method in connection with geometric ray tracing was first developed by Wendling *et al.* (1979) for hexagonal ice columns and plates. Takano and Liou (1995) further innovated a hit-and-miss Monte Carlo method to trace photons in complex ice crystals, including absorption and polarization.

Let a bundle of parallel rays, representing a flow of photons, be incident on a crystal from a direction denoted by a set of two angles with respect to the crystal principal axis. Consider a plane normal to this bundle of incident rays and the geometric shadow of a crystal projected onto this plane. Further, let a rectangle (defined by X and Y) enclose this geometric shadow such that the center of this

rectangle coincides with the center of the crystal. One of the sides, X, is parallel to the geometric shadow of the crystal principal axis. A point (x_i, y_i) is selected inside this rectangle using random numbers, RN, whose range is from 0 to 1 such that

$$x_i = X\left(\mathrm{RN} - \frac{1}{2}\right), \tag{19a}$$

$$y_i = Y\left(\mathrm{RN} - \frac{1}{2}\right). \tag{19b}$$

In this manner, x_i is from $-X/2$ to $X/2$, whereas y_i is from $-Y/2$ to $Y/2$. If the point is inside the geometric shadow, it is regarded as an incident point on the crystal. Otherwise it is disregarded. If there are more than two crystal planes for a photon, the point closer to the light source is regarded as the incident point. The coordinates of an incident point (x_i, y_i) can be transformed to the coordinates (x, y, z) with respect to the body-framed coordinate system using the method described by Takano and Asano (1983) for efficient geometric ray-tracing procedures. Once the incident coordinates are determined, the photons are traced with a hit-and-miss Monte Carlo method. The Fresnel reflection coefficients, R_l and R_r, are first calculated and compared with a random number, RN. If $(|R_l|^2 + |R_r|^2)/2$ is greater than RN, the photon is reflected. Otherwise, it is transmitted. When a photon traverses a particle, it can be absorbed. One can account for absorption by means of stochastic procedures. When a photon enters a crystal, an absorption path length l_a is generated with a random number such that

$$\mathrm{RN} = \exp(-2kN_{\mathrm{i}}l_a), \qquad \text{i.e., } l_a = -\ln\left(\frac{\mathrm{RN}}{2kN_{\mathrm{i}}}\right). \tag{20}$$

The random number represents the probability of the transmission of a photon. The absorption path length l_a denotes a distance traversed by a photon in the crystal before the photon is absorbed. An actual path length, l, between an incident point and the next internal incident point can then be calculated on the basis of Snell's law and the specific ice crystal geometry. The transmission is then given by $T = \exp(-k_i l)$. If $T \leq \mathrm{RN} \leq 1$, then the photons associated with these RNs are absorbed. Equivalently, if l is greater than l_a, then the photon is absorbed. Otherwise, it is transmitted without absorption. This procedure is repeated whenever photons travel inside the crystal.

After a photon is transmitted out of the crystal or reflected externally, it can reenter the crystal depending on the crystal shape. In this case, a new incident direction can be calculated using the direction cosine of the scattered beam. The new incident coordinates can also be determined from the new incident direction and the coordinates of an emergent point of the photon on the crystal surface. The foregoing procedure is repeated until the photon escapes from the crystal.

When a photon reenters the crystal, the scattering angle and the scattering matrix are computed with respect to the original incident direction. In the conventional method, the number of scattered photons per unit solid angle, $2\pi \sin\Theta\,\Delta\Theta$, is counted as the phase function. The single-scattering albedo is obtained from the ratio of the number of scattered photons to the number of incident photons. The Monte Carlo method allows us to treat complicated ice crystals effectively and can be employed in connection with the improved geometric ray tracing.

The surface of ice crystals may not be exactly smooth particularly if they undergo collision processes. Also, a careful examination of some polycrystalline ice crystals reveals rough structures on the surfaces (Cross, 1968). Halo and arc patterns that are absent from some cirrus clouds could be caused by deviations of the ice crystal surfaces from defined hexagonal structures. Incorporation of some aspects of the ice crystal surface roughness in geometric ray tracing has been recently undertaken by Takano and Liou (1995), Muinonen *et al.* (1996), Macke *et al.* (1996b), and Yang and Liou (1998a). Our approach follows the idea developed by Cox and Munk (1954) for wavy sea surfaces. A rough surface may be thought of as consisting of a number of small facets that are locally planar and randomly tilted from the flat surface. We may use a two-dimensional Gaussian probability function to define the surface tilt as follows:

$$p(z_x, z_y) = \frac{1}{\pi\sigma^2} \exp\left[-\frac{z_x^2 + z_y^2}{\sigma^2}\right], \tag{21a}$$

with

$$z_x = \frac{\partial z}{\partial x} = \left[(\cos\theta)^{-2} - 1\right]^2 \cos\varphi, \tag{21b}$$

$$z_y = \frac{\partial z}{\partial y} = \left[(\cos\theta)^{-2} - 1\right]^2 \sin\varphi, \tag{21c}$$

where z_x and z_y are the slopes defined for a facet of rough surface along two orthogonal directions, θ and φ are the local polar angles defining the position of the tilt of the surface facet, and σ is a parameter controlling the degree of roughness. In general, effects of the surface roughness on ice particles are to smooth out the scattering maxima that occur in the phase function (see Fig. 4).

B. Finite Difference Time Domain Method

The geometric ray-tracing method with a modification in the mapping of the near field to the far field can be applied to size parameters on the order of about 15–20. We have developed the finite difference time domain (FDTD) method for light scattering by small ice crystals with specific applications to size parameters smaller than about 20 (Yang and Liou, 1995, 1996b; Chapter 7). Details of this

method have been elaborated on in Chapter 7. For the continuity of this presentation, however, we shall address the physical fundamentals of the methodology.

The FDTD technique is a direct implementation of the Maxwell curl equations to solve the temporal variation of electromagnetic waves within a finite space containing the scatterer given by

$$\nabla \times \mathbf{E}(\mathbf{r}, t) = -\frac{\mu}{c} \frac{\partial \mathbf{H}(\mathbf{r}, t)}{\partial t}, \tag{22a}$$

$$\nabla \times \mathbf{H}(\mathbf{r}, t) = \frac{\varepsilon}{c} \frac{\partial \mathbf{E}(\mathbf{r}, t)}{\partial t} + \frac{4\pi}{c} \sigma \mathbf{E}(\mathbf{r}, t), \tag{22b}$$

where μ, ε, and σ are the permeability, permittivity, and conductivity of the medium, respectively.

First, the three-dimensional scatterer must be discretized by a number of suitably selected rectangular cells, referred to as grid meshes, at which the optical properties are defined. Discretizations are subsequently carried out for the Maxwell curl equations by using the finite difference approximation in both time and space. The propagation and scattering of the excited wave in the time domain can be simulated from the discretized equations in a manner of time-marching iterations.

Second, in numerical computations, scattering of the electromagnetic wave by a particle must be confined to finite space. It is therefore required in the application of the FDTD technique to impose artificial boundaries so that the simulated field within the truncated region would be the same as that in the unbounded case. Implementation of an efficient absorbing boundary condition to suppress spurious reflections is an important aspect of the FDTD method associated with numerical stability and computer time and memory requirements.

Third, the solution of the finite difference analog of the Maxwell curl equations is in the time domain. To obtain the frequency response of the scattering particle, we require an appropriate transformation. The discrete Fourier transform technique can be employed to obtain the frequency spectrum of the time-dependent signals if a Gaussian pulse is used as an initial excitation. Correct selection of the pulse is required to avoid numerical aliasing and dispersion.

Finally, mapping of the near-field results to the far field must be performed to derive the scattering and polarization properties of the particle. A surface integration or a volume integration technique, mentioned in Section II.A.2, can be employed to obtain the far-field solution. Fundamental problems of the FDTD method in numerical calculations include the staircasing effect in approximating the particle shape and the absorbing boundary condition used to truncate the computational domain. We have shown in Chapter 7 that the FDTD approach can be applied to size parameters smaller than about 20 with adequate accuracies.

C. Essence of the Unified Theory and Comparison with Measurements

It is unlikely that one specific method can be satisfactorily used to tackle the scattering of light by nonspherical ice crystals covering all size parameters. However, by unifying the improved geometric ray-tracing and FDTD methods discussed previously, we are now in a position to resolve the intricate problems involving light scattering and absorption by nonspherical ice crystals. This approach is referred to as the unified theory for light scattering by ice crystals covering all sizes and shapes that commonly occur in the atmosphere. Demonstration of this unified theory is shown in Fig. 2 in terms of the extinction efficiency as a function of size parameter kL for randomly oriented columns, where L is the column length. The improved geometric optics method breaks down at size parameters smaller than about 15, whereas the FDTD method is computationally reliable for size parameters smaller than about 20 because of numerical limitations. Also illustrated is a verification of the improved geometric ray tracing for size parameters from 15 to about 20.

Figure 3 displays the commonly occurring ice crystal shapes in cirrus clouds generated from computer programs, along with the phase function patterns at a wavelength of 0.63 μm computed from the geometric ray-tracing method. The size parameters for these ice crystals are on the order of 100. Irregular shapes,

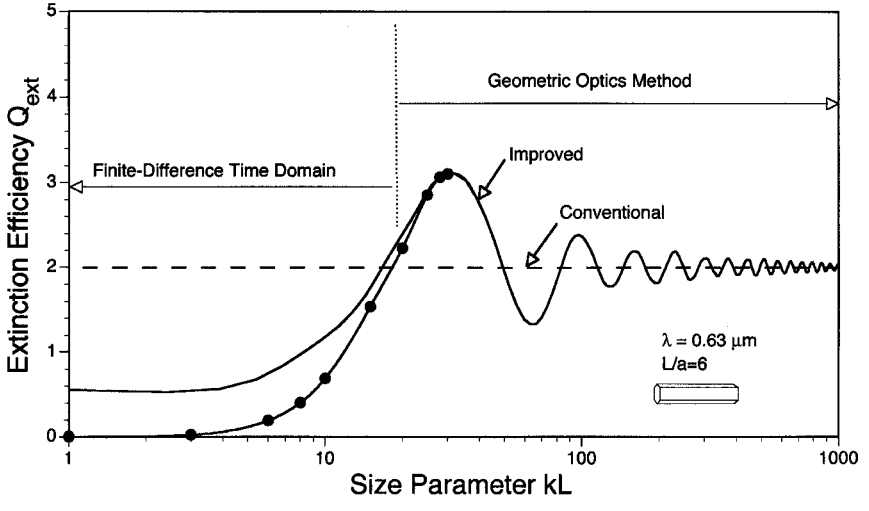

Figure 2 Presentation of a unified theory for light scattering by ice crystals using the extinction efficiency as a function of size parameter as an example (see text for further explanations).

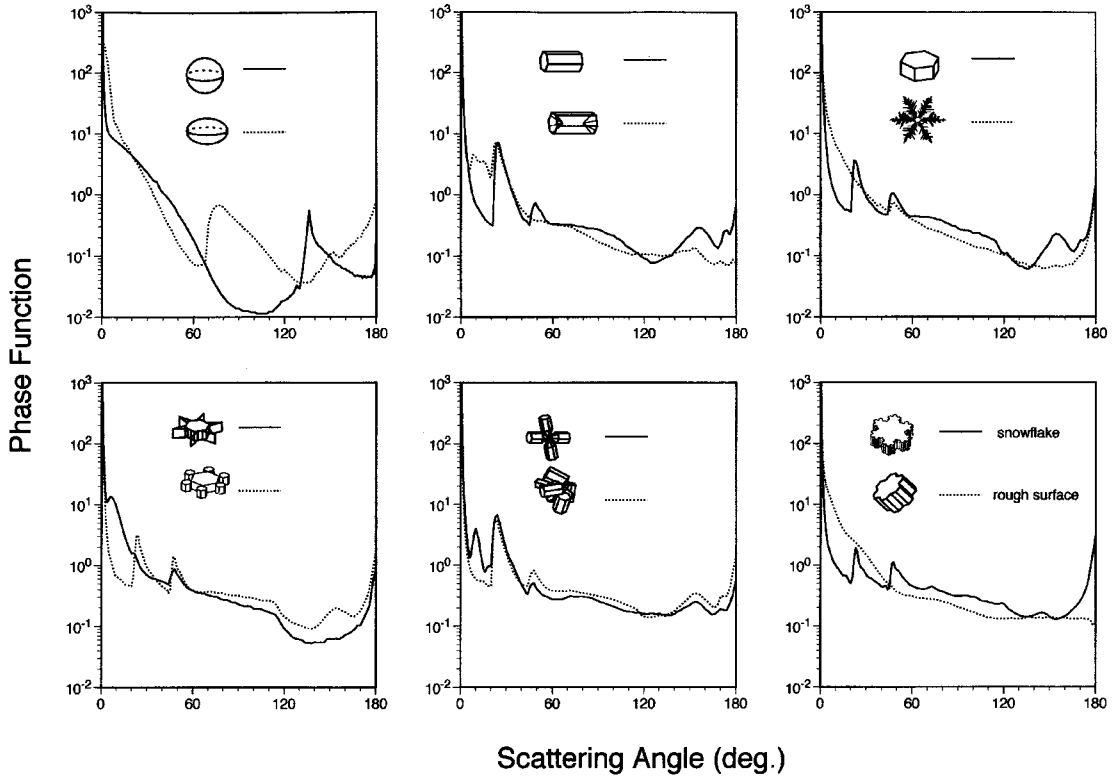

Figure 3 Commonly occurring ice crystal shapes in cirrus clouds generated from the computer program, along with the phase function patterns for the 0.63-μm wavelength computed from a geometric ray-tracing method. The patterns for snowflakes, dendrites, and plates with attachments are produced from a fractal shape generation program. Results for a sphere and spheroid are also shown for comparison purposes.

such as hollow column, dendrite, and fernlike plate, and rough surface ice crystals do not produce well-defined halo patterns that are common to hexagonal-based crystals such as bullet rosettes and aggregates. Results for small size parameters less about 20 can be computed from the FDTD method.

Measurements of the scattering and polarization patterns for ice crystals have been performed in cold chambers (e.g., Sassen and Liou, 1979a; Volkovitskiy *et al.*, 1980). Desirable ice crystal sizes and shapes, however, are difficult to generate and sustain for a period of time to perform light-scattering experiments. A light-scattering experimental program has been recently conducted using hexagonal icelike crystals as measured in the analog manner so that optical experiments can be performed over a relatively long period of time for complex-shaped particles (Barkey *et al.*, 1999). The experiment consisted of a polarized laser beam at $\lambda = 0.63$ μm and an array of 36 highly sensitive photodiode detectors arranged between the scattering angles 2.8° and 177.2° mounted in a linear array on a half dome, which can rotate to vary the azimuthal angle. After careful calibration and signal acquisition, this system was used to measure the phase functions for a glass sphere and a glass fiber configured to scatter light like an infinite cylinder. The experimental results match closely those computed from the Lorenz–Mie theory. The crystals used were made out of sodium fluoride (NaF), which has an index of refraction (1.33) close to ice in the visible. The crystal was mounted on top of a small pedestal and its orientation position was controlled by a rotator. Angular integrations in the experiment can follow the computational procedures in theory.

Figure 4a shows a comparison between measurements and theory for an aggregate that was assembled from NaF columns with small glass fiber attachments glued onto small holes. To simulate random orientation, a 1° increment was used for all possible orientation angles. General agreement between measurements and theory is shown but with several discrepancies. Most notable is that the experimental results are lower than the theory in backscattering directions, which are dominated by internal reflections. This difference could be caused by absorption of small glass fibers and glues that connect the columns. Comparison results for a rough-surface plate are shown in Fig. 4b. All eight sides were sanded with small scratches evenly distributed across the crystal surface. Between 25° and 180° scattering angles, the measurements closely follow the theoretical results. For scattering angles less than 20°, the experimental results are higher, however. The scanning electron photomicrographs reveal features on the roughened crystal surface on the order of 0.5–1 μm. More light could have been scattered through them as compared with the defined cross-sectional area used in diffraction calculations.

The electrodynamic levitation technique has also been used recently to suspend and grow an individual ice crystal for light-scattering experiments (Bacon *et al.*, 1998). The apparatus consists of an electrodynamic balance with an internally mounted thermal diffusion chamber, a laser beam, a 1024-element linear photo-

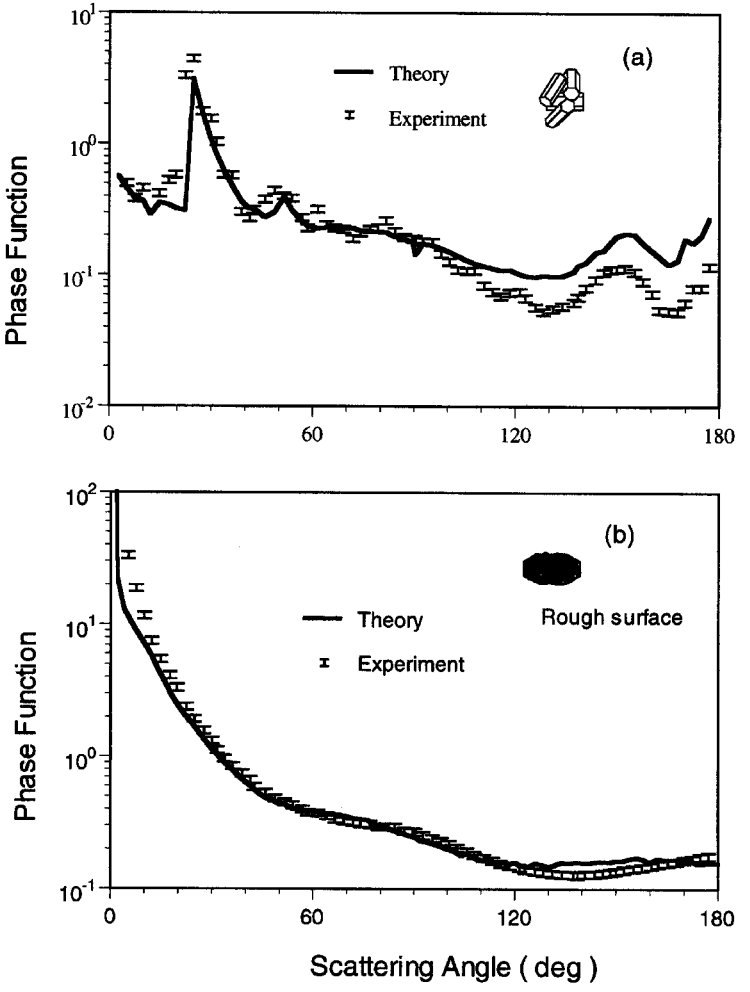

Figure 4 Phase functions for randomly oriented aggregate and rough surface plate crystals made from NaF with an index of refraction of 1.33 in the visible. The experiment used a polarized laser beam at $\lambda = 0.63$ μm as a light source and the positions of the detector and the crystal were controlled by automatic mechanical devices (Barkey *et al.*, 1999). The theoretical results are derived from the geometric ray-tracing/Monte Carlo method.

diode array, and two cameras for top and side views of the ice crystal. Shown in Fig. 5 are experimental results for two ice crystal sizes and shapes defined by the depicted photos (courtesy of N. J. Bacon). Theoretical results computed from conventional geometric ray tracing, which does not account for phase interferences,

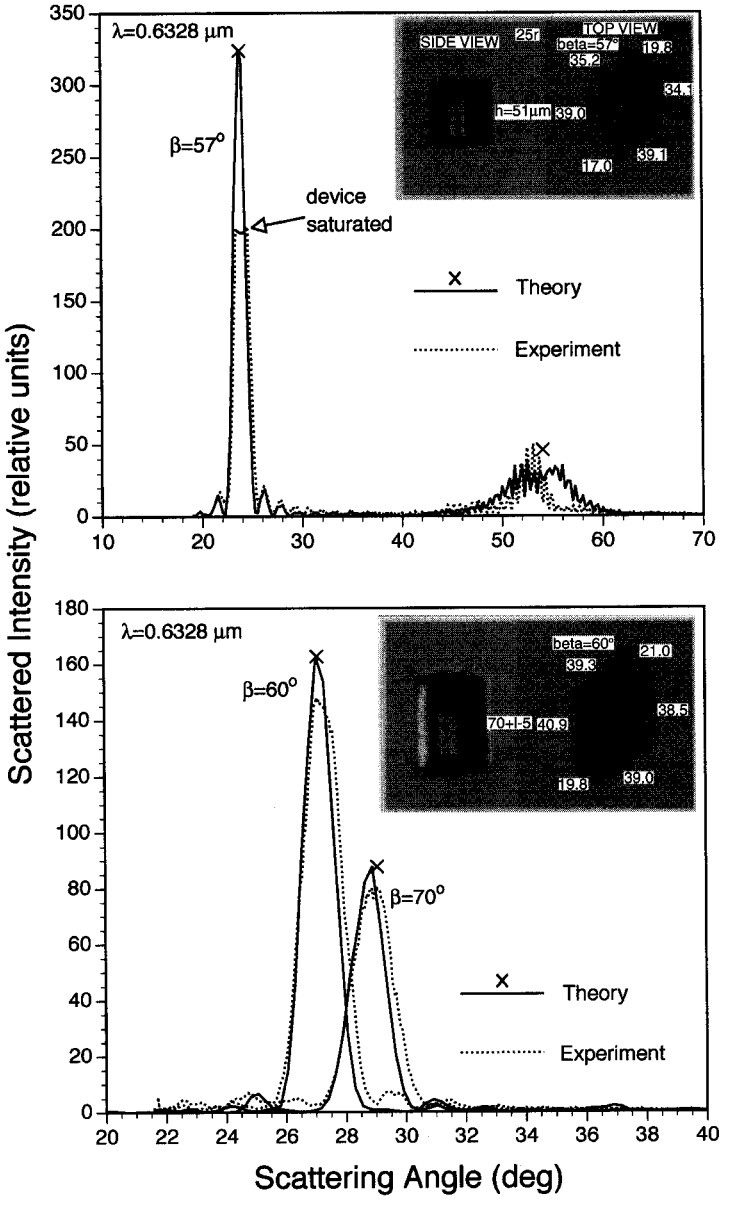

Figure 5 Phase function measurements for a single ice crystal suspended by the electrodynamic levitation technique (Bacon *et al.*, 1998). The sizes and shapes are determined from the top and side views of two cameras. The angle β denotes the ice crystal orientation with respect to the incident laser beam. Theoretical results are computed from the conventional ($\times$) and modified geometric ray-tracing methods.

show discrete maxima associated with the halo pattern. The modified geometric optics method generates closely matched patterns, except some deviations in the 55° scattering angle region in the top diagram. Differences between theoretical and experimental results can be attributed to the uncertainty in the measurement of the ice crystal size (~4 μm) and in the computation of the near field based on the geometric ray-tracing approximation.

III. APPLICATION TO REMOTE SENSING AND CLIMATE RESEARCH

Determination of the composition and structure of clouds and aerosols from the ground, the air, and space based on remote sensing is an important task in climate studies. In the following, we wish to demonstrate the applicability of the basic scattering, absorption, and polarization data for nonspherical ice crystals to various types of remote sensing of cirrus clouds and to climate studies.

A. Bidirectional Reflectance

Solar radiances reflected from clouds can be used to determine their composition and structure. The nondimensional bidirectional reflectance, the ratio of reflected and incident radiances for given positions of the Sun and observer and an underlying surface, is primarily a function of the cloud optical depth and particle size and shape. Development of reliable remote-sensing techniques from satellites for the detection of cirrus clouds and retrival of their optical and microphysical properties using bidirectional reflectances must begin with an understanding of the fundamental scattering and absorption properties of ice particles.

Figure 6 shows measurements of the bidirectional reflectances of cirrus that were obtained with the scanning radiometer on board *ER-2* over Oklahoma on November 24 and 25, 1991, presented by Spinhirne *et al.* (1996), who also derived the best-fit cloud optical depths and surface albedos from concurrent lidar and spectral radiometric observations. For interpretation, we used a typical cirrostratus size distribution having a mean effective size of 42 μm and three ice crystal models: spheres, defined hexagons, and irregular ice particles (aggregates with rough surfaces). For the same optical depth, ice spheres reflect much less radiation than nonspherical ice crystals. The best matches for the three cases presented appear to be irregular particles. Because the measured data were about 20° apart, it is possible that some scattering maxima could be missed in the observations. It appears that the ice crystals in these developed cirrus must contain a combination of hexagonal and irregular ice crystals. In the visible, the bidirectional reflectance

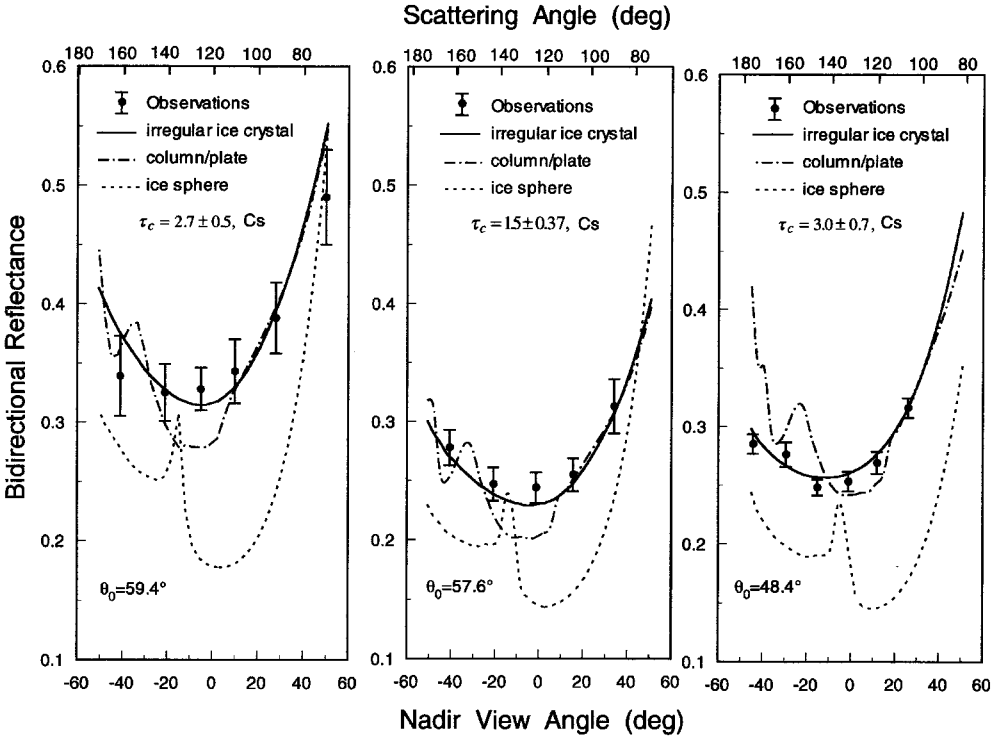

Figure 6 Measurements of visible bidirectional reflectances of cirrus obtained from the scanning radiometer on board *ER-2* over the area of Oklahoma on November 24 and 25, 1991 (Spinhirne *et al.*, 1996), and interpretations using light-scattering results for spheres, defined hexagons, and aggregates with rough surfaces based on the adding–doubling method for radiative transfer. A typical ice crystal size distribution with a mean effective size of 42 μm and predetermined optical depths are employed in the interpretation.

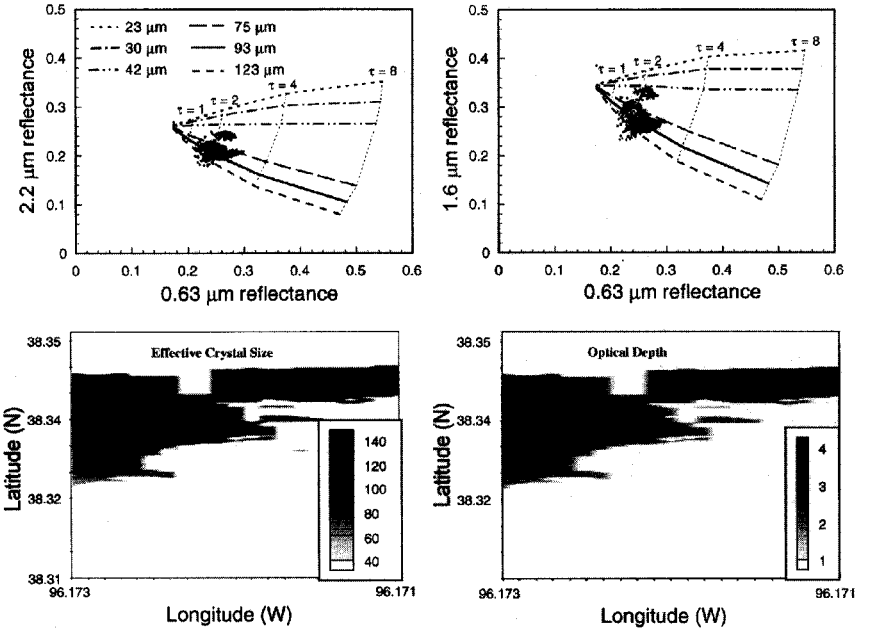

Figure 7 Correlations of the bidirectional reflectances in the wavelength domains of 0.63/1.6 μm and 0.63/2.2 μm. Six representative ice crystal size distributions with mean effective sizes ranging from 23 to 123 μm and optical depths from 0.1 to 8 are used in the construction of these curves. The viewing geometry includes $\theta_0 = 31.5°$, $\theta_0 = 12.5°$, and $\Delta\phi = 100°$. Also shown are the bidirectional reflectances obtained from MAS during the SUCCESS experiment on April 26, 1996. The bottom panels illustrate the retrieved optical depth and ice crystal mean size based on a statistical searching method (Rolland and Liou, 1998).

is largely dependent on the optical depth and ice crystal shape. The size information has been found from measurements at near infrared wavelengths where substantial absorption by ice occurs (King *et al.*, 1997).

In the following, we show the potential of determining the optical depth and ice crystal size based on correlation of bidirectional reflectance data in the domain of $\lambda = 0.63/1.6$ μm and $0.63/2.2$ μm (Fig. 7). In the construction of the correlation diagram, six representative midlatitude ice crystal size distributions were used along with optical depths ranging from 0.1 to 8. The mean effective size ranges from 23 to 123 μm. The adding–doubling method for radiative transfer was employed to compute the bidirectional reflectances for cirrus cloud layers. Also shown are bidirectional reflectances obtained from the MODIS Airborne Simulator (MAS) for a sample viewing geometry occurring on April 26, 1996, during the SUCCESS experiment (Rolland and Liou, 1998). The retrieved opti-

cal depth ranges from about 2 to 4 and the retrieved mean effective ice crystal sizes are about 40–120 μm, as shown in the following maps. Validation of these retrievals has not been made at this point, however.

B. Linear Polarization of Reflected Sunlight

Next, we present the applicability of the scattering data for nonspherical ice crystals to the interpretation of polarization of the reflected sunlight from cirrus clouds. Figure 8 shows the linear polarization pattern in the solar principal plane as a function of scattering angle that was measured from a cirrus cloud using a wavelength of 2.22 μm (Coffeen, 1979) at which the Rayleigh scattering contribution is minimum. The measured polarization values are less than about 6% and are positive from 50° and 150° scattering angles. The theoretical results based on the adding–doubling radiative transfer program (Takano and Liou, 1989b) include spheres, columns, plates, and a mixture of dendrites, bullet rosettes, and plates.

Results from the spherical model deviate significantly from observations in which the rainbow feature does not exist. For plates and columns, negative polarization results in the scattering angle region from 20° to 40° produced by halo patterns show general agreement with the observed data. The results for columns appear to match the observations, except in the backscattering direction from about 150° to 180°. With the inclusion of dendrites the backscattering polarization decreases and there is a general agreement between theoretical results and observed data in the entire scattering-angle range. It appears that the polarization patterns of the reflected sunlight can be used to infer the shape of cloud particles, which otherwise cannot be accomplished by other remote-sensing techniques.

C. Lidar Backscattering Depolarization

The depolarization technique using lidar backscattering returns has been developed to differentiate between ice and water clouds. It is based on the fundamental scattering properties of nonspherical ice crystals and spherical water droplets. The incident polarized light beam from spheres will retain its polarization state in the backscattering direction, if multiple scattering can be neglected. However, a cross-polarized component, referred to as depolarization, will be produced by nonspherical particles because of their deviation from the spherical geometry. In the geometric optics region, Liou and Lahore (1974) showed that depolarization is the result of internal reflections and refractions by hexagonal ice particles. To

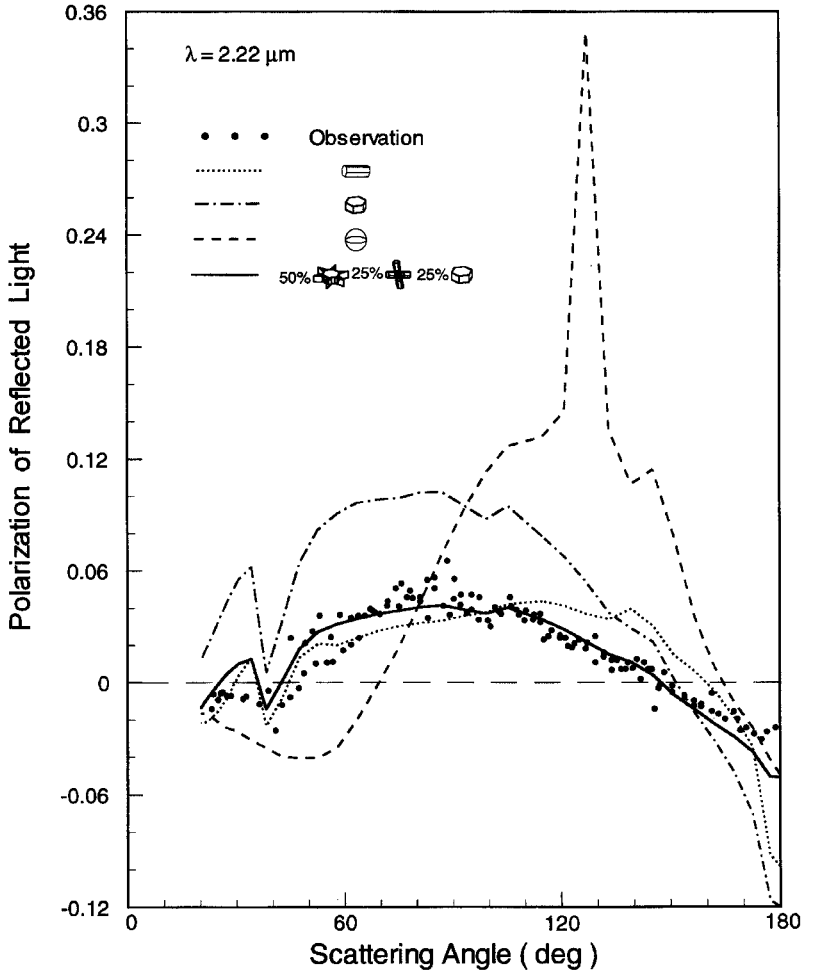

Figure 8 Linear polarization of sunlight reflected from a cirrus cloud measured at the 2.2-μm wavelength (Coffeen, 1979). The solar zenith angle is 70°. The theoretical polarization results are computed for ice spheres, columns, plates, and a mixture of dendrites, bullet rosettes, and plates as a function of the scattering angle.

quantify the amount of depolarization, a parameter called the depolarization ratio, defined as the ratio of the cross-polarized return power to the return power of the original polarization state, is introduced. It has been used to differentiate between ice and water clouds, as well as to determine some aspects of the physical characteristics of ice clouds (Sassen, 1991; Chapter 14).

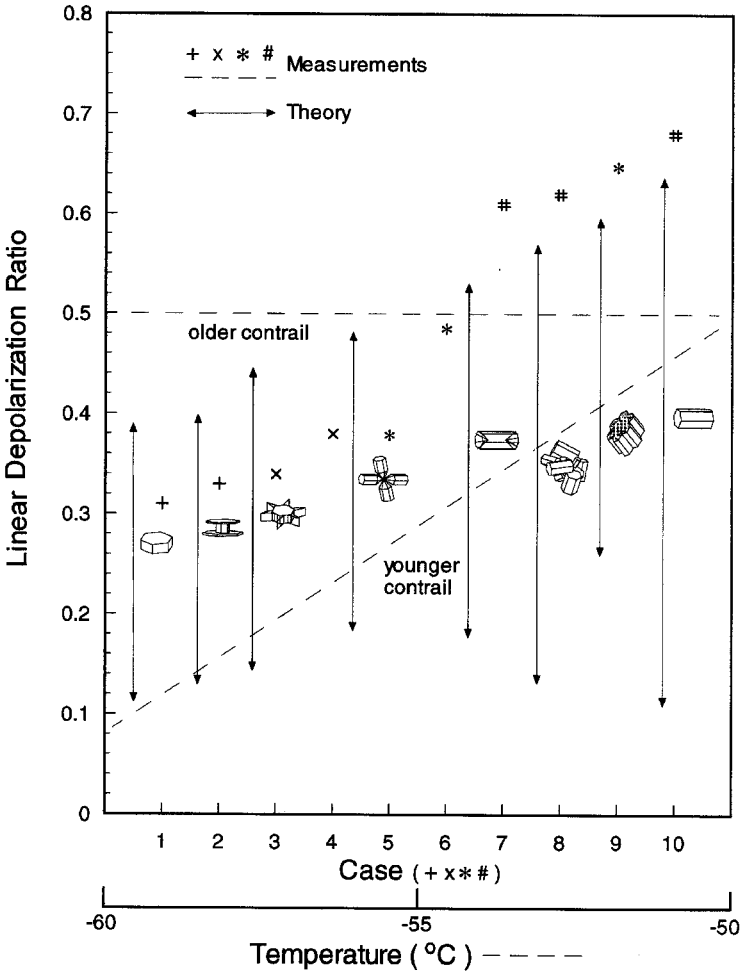

Figure 9 Depolarization ratios determined from high-resolution polarization lidar for contrail cirrus (Sassen and Hsueh, 1998, case; Freudenthaler *et al.*, 1996, temperature) and computed from the unified theory for light scattering by ice crystals with shapes ranging from single and double plates, solid and hollow columns, dendrites, bullet rosettes, aggregates, and irregular surface particles, the sizes of which span from a few micrometers to the geometric optics limit.

Figure 9 shows the depolarization ratios determined from high-resolution 0.532/1.06-μm polarization lidar for contrail cirrus presented by Sassen and Hsueh (1998) and Freudenthaler *et al.* (1996). The former authors showed that the lidar depolarization ratio in persisting contrails ranged from about 0.3 to 0.7,

whereas the latter authors observed this ratio from 0.1 to 0.5 for contrails with temperatures ranging from −60° to −50°C depending on the stage of their growth. For interpretation, we have carried out backscattering depolarization calculations for various sizes and shapes displayed in this figure employing the unified theory for light scattering by ice crystals described in Section II. The vertical bars indicate the results for ice crystals of a few micrometers to the geometric optics region. Depolarization generally becomes larger for larger ice particles and reaches a maximum of about 0.6 for size parameters in the geometric optics limit. One exception is for columns, which produce a depolarization of about 0.65 for size parameters of about 10 because of resonance effects.

D. Information Content of 1.38-μM and Thermal Infrared Spectra

Water vapor exhibits a number of absorption bands in the solar spectrum. Bidirectional reflectance at the top of the atmosphere in these bands will contain information of high-level clouds. Specifically, the 1.38-μm band has been found to be useful for the detection of cirrus clouds (Gao and Kaufman, 1995). The line spectra in this band have also been shown to contain rich information on the composition and structure of clouds and were a subject for a small-satellite proposal (Liou *et al.*, 1996).

To investigate the line formation in cirrus in the 1.38-μm band, we use a radiation model with a 1-cm^{-1} resolution containing 10 equivalent absorption coefficients based on the correlated k-distribution method for water vapor and other greenhouse gases derived from the updated 1996 HITRAN data (Liou *et al.*, 1998). The adding–doubling radiative transfer program including all Stokes parameters is used to perform the transfer of monochromatic radiation in vertically inhomogeneous atmospheres decomposed into a number of appropriate homogeneous layers. This program incorporates line absorption, scattering and absorption by nonspherical ice crystals, Rayleigh and background aerosol scattering, and surface reflection, and accounts for both direct solar flux and thermal emission contributions. In the calculations, we employ cirrostratus and cirrus uncinus models having mean effective ice crystal sizes of 42 and 123 μm, respectively, with a shape composition of 50% aggregates/bullet rosettes, 25% hollow columns, and 25% plates.

Figure 10a illustrates the bidirectional reflectances in the 1.38-μm water vapor line spectrum from 6600–7500 cm^{-1} for clear and cirrus cloudy conditions. The line structure of the water vapor absorption exhibits significant fluctuations. At about 7100–7400 cm^{-1}, the reflectances from the clear atmosphere are extremely small as a result of strong water vapor absorption. Multiple scattering produced by ice particles contributes to the strength of reflectances in the line

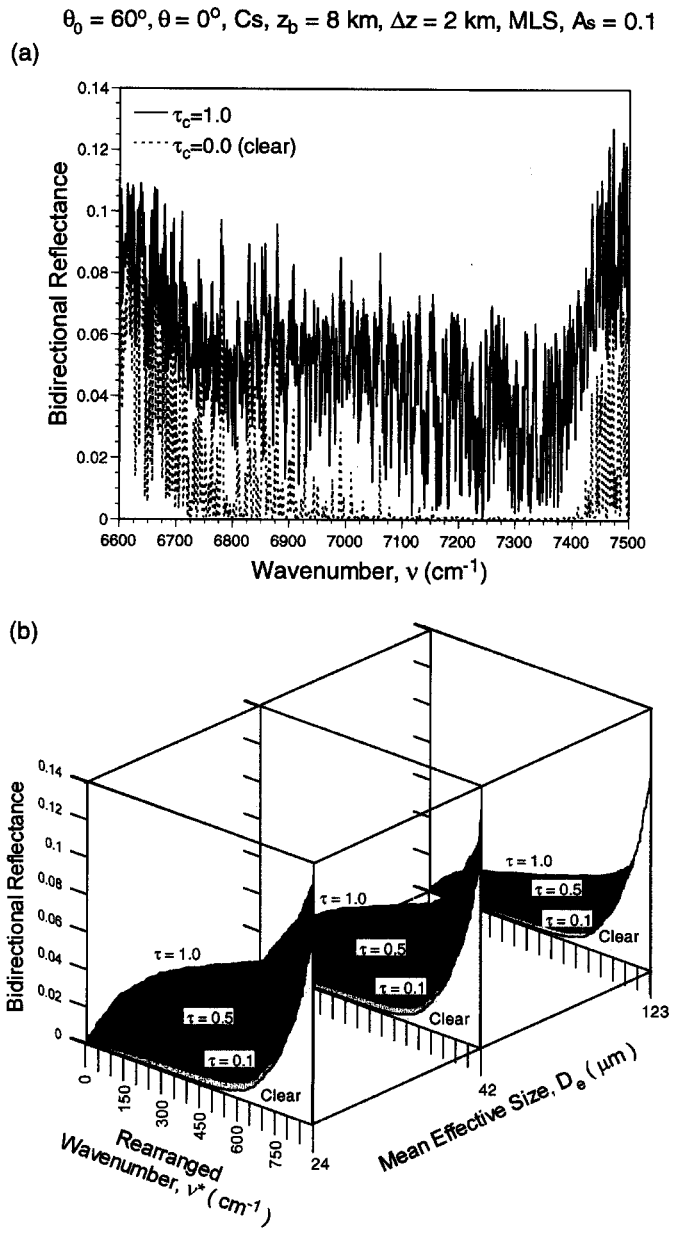

Figure 10 (a) Bidirectional reflectances for clear and cirrus cloudy atmospheres as a function of wavenumber in the 1.38-μm water vapor band. (b) Monotonically increasing bidirectional reflectances as a function of rearranged wavenumber in the domain of optical depth and mean effective ice crystal size. The solar and emergent zenith angles are denoted in the figure and the calculations were carried out in the solar principal plane.

wing regions. Figure 10b shows the reflectance spectra whose wavenumbers are ordered according to their magnitudes so that monotonically increasing functions are displayed in the domain of optical depth and mean effective ice crystal size. Low values indicate that the reflectances are associated with line centers, whereas high values are related to line wings. Reflectances are dependent on the optical depth and ice crystal size, as clearly demonstrated in this example. Consequently, a retrieval procedure can be constructed for the determination of these two parameters. Moreover, we find that the cloud position can also be inferred from the spectra because the reflectances are determined by the amount of water vapor above the cloud. The preceding example clearly demonstrates that the 1.38-μm line spectra contain rich information about the cirrus composition and structure. Of course, the question of uniqueness of the solution of cloud parameters within the broad range of spectral lines is one that requires further investigations and numerical experimentations.

Information on thin cirrus in the tropics has been noted from the analysis of satellite Infrared Radiation Interferometer Spectrometer (IRIS) data (Prabhakara *et al.*, 1993), particularly in the 8–12-μm window region. Recent technological advancements have led to the development of the High-Resolution Interferometer Sounder (HIS), a Michelson interferometer covering a broad spectral region in the infrared (3.5–19 μm) with high spectral and spatial resolutions (Smith *et al.*, 1998). Information on thin cirrus containing small ice crystals appears between $\lambda = 10$ and 12 μm. Interpretation of the line structure in the thermal infrared for cirrus cloudy atmospheres and exploration of the information content with respect to the cloud optical depth, ice crystal size, and position would be an exciting project.

In summary, because of the spatial and temporal variabilities of ice crystal sizes and shapes in cirrus clouds, remote sensing of their optical and microphysical properties from space presents an unusual challenge in atmospheric sciences.

E. Solar Albedo

Reflection of solar radiation by clouds determines the amount of solar energy absorbed within the atmosphere and by the surface. Thus, understanding the broad-band solar albedo (reflection) is fundamental in the analysis of the cloud radiative forcing associated with climate studies. We wish to illustrate the importance of the nonsphericity of ice particles on the interpretation of observed solar albedo determined from radiometric measurements. Figure 11 shows the broad-band solar albedo as a function of the ice water path (IWP) derived from broad-band flux aircraft observations for cirrus clouds during the FIRE experiment in Wisconsin, October–November, 1986 (Stackhouse and Stephens, 1991). The extensions of the vertical and horizontal lines through the data points represent the uncertainty of measurements.

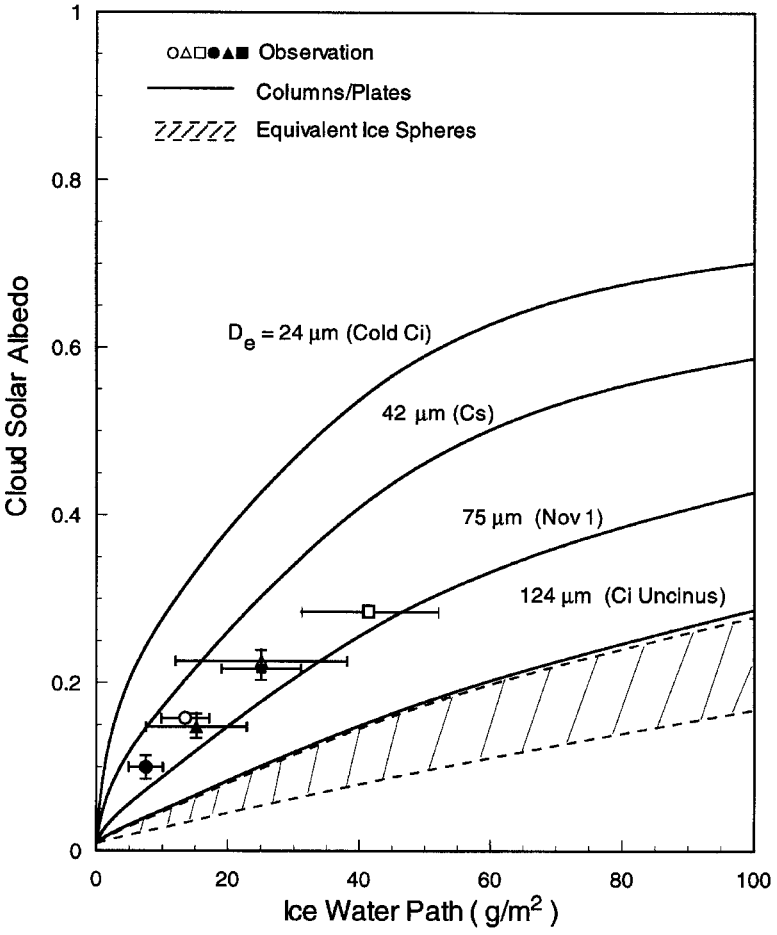

Figure 11 Solar albedo as a function of ice water path determined from broad-band flux observations from aircraft for cirrus clouds that occurred during the FIRE experiment, Wisconsin, November–December, 1986 (Stackhouse and Stephens, 1991). The solid lines represent theoretical results computed from a line-by-line equivalent solar model using observed ice crystal sizes and shapes for a range of mean effective ice crystal diameters. The dashed lines are corresponding results for equivalent spheres.

The solid lines are theoretical results computed from the line-by-line equivalent solar radiative transfer model mentioned previously using a set of observed ice crystal size distributions for columns and plates. The dashed lines denote the results based on these size distributions converted into equivalent spheres. Regardless of the input parameters for spheres, the theoretical results significantly

underestimate the observed values primarily because of the nature of stronger forward scattering for spherical particles and stronger absorption for spheres at near infrared wavelengths. Using the mean effective ice crystal size defined in Liou *et al.* (1998), we show that the size that best fits the observed data lies between 50 and 75 μm, typical ice crystal sizes at the top portion of midlatitude cirrus cloud systems.

Further, we have also investigated from a theoretical perspective the effects of ice crystal shape on solar albedo by using a mean effective size of 16 μm, representing a typical ice crystal size for contrail cirrus. In this study, four shapes are used in which bullet rosettes have both smooth and rough surfaces. Cloud albedo, not shown here, becomes progressively smaller for hollow columns, plates, and equal-area spheres relative to that of bullet rosettes, primarily because their asymmetry parameters become increasingly larger to allow stronger forward scattering to take place. The effect of ice crystal surface roughness does not appear to alter the solar albedo values for nonspherical particles. It does, however, affect the phase function pattern, a critical parameter in remote-sensing applications.

F. Temperature Sensitivity to Ice Crystal Nonsphericity

Many dynamic and thermodynamic factors and feedbacks affect temperature perturbations. Nevertheless, we wish to demonstrate that the scattering and absorption properties of nonspherical ice crystals are relevant and important in the modeling of the role of clouds in climate. The potential effect of ice crystal nonsphericity in light scattering on climatic temperature perturbations is studied by using a one-dimensional cloud–climate model developed by Liou and Ou (1989). Perturbation calculations were performed by varying the cloud cover and IWP for a typical cirrostratus cloud model with a thickness of 1.7 km and a base height of 9 km. Cloud positions and covers for middle and low clouds were prescribed and other parameters in the model remained unchanged in the perturbation runs. The radiative properties of columns/plates and area-equivalent ice spheres were incorporated into the climate model to investigate sensitivity to the surface temperature change. The present climate condition is defined at 288 K, which corresponds to a cirrus cloud cover of 20% and an IWP of 20 g/m^2 based on the column/plate model.

The left panel of Fig. 12 shows the variation of surface temperature as a function of cloud cover when the IWP is fixed. Because the greenhouse effect produced by the trapping of thermal infrared radiation outweighs the solar albedo effect, increasing the cloud cover increases the surface temperature. If a spherical model is used, a significant increase of the surface temperature occurs because

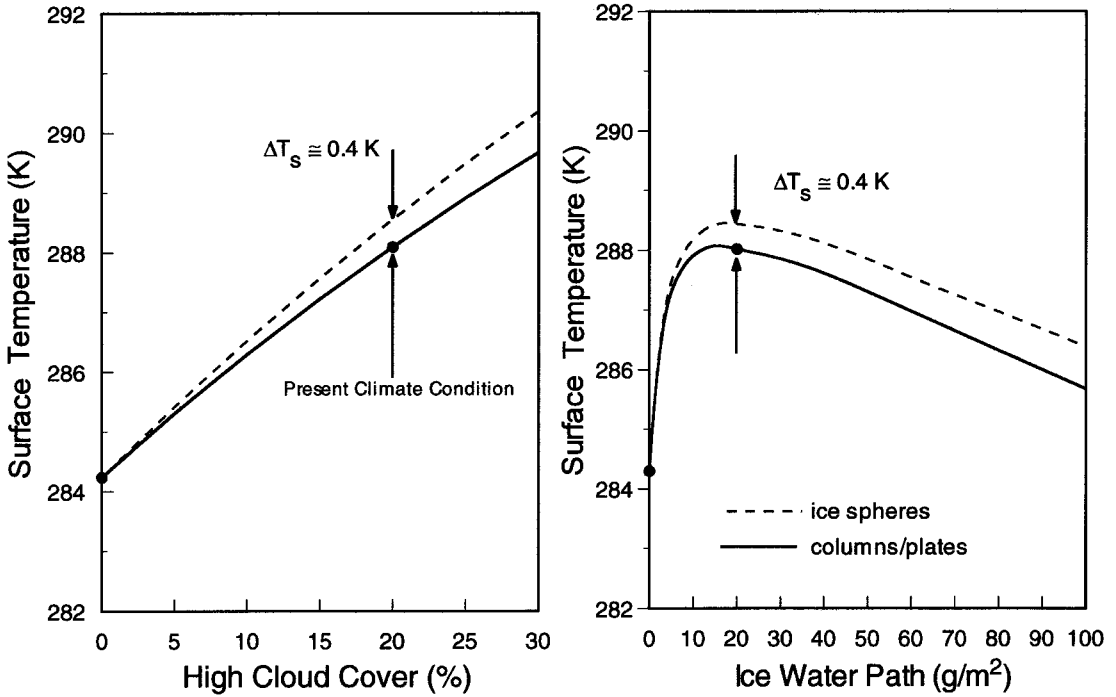

Figure 12 Surface temperatures determined from a one-dimensional cloud and climate model using a radiative transfer parameterization based on the scattering and absorption properties of hexagonal columns/plates and equivalent ice spheres. The model has a present climate condition corresponding to the surface temperature of 288 K involving a typical cirrostratus located at 9 km with a thickness of 1.7 km and an ice water content of 10^{-2} g/m^3 and the cirrus has 20% fractional coverage. Perturbations are performed for both cloud cover and IWP.

equivalent spheres reflect less solar radiation as shown in Fig. 11. At the present climate condition, the increase amounts to about 0.4 K, which appears to be substantial. Variation of the IWP when the cloud cover is fixed is shown in the right panel of Fig. 12. An increase of the surface temperature occurs at IWPs up to 15 g/m^2 after which a decrease occurs. This is because an increase in the infrared (IR) emissivity is relatively smaller as compared with an increase in the solar albedo, thereby leading to cooling effect. Using the spherical model, the cloud radiative forcing increases by about a factor of 2 because of a reduction in the solar albedo. For this reason, larger surface temperatures are produced relative to the case involving the column/plate model.

In view of the preceding discussion, a sufficient sensitivity of climatic temperature perturbations can be observed when the shape of ice particles (spheres vs hexagons) is accounted for in radiative transfer calculations. Thus a physically based cloud microphysical model is required in the parameterization of the radiative properties of cirrus clouds for climate models.

IV. SUMMARY

We have presented a unified theory for light scattering by ice crystals of all sizes and shapes that can be defined mathematically or numerically. This theory is a combination of a geometric optics approximation for size parameters larger than about 20 and a finite difference time domain method for size parameters smaller than about 20. Conventional geometric ray tracing was first reviewed, followed by a discussion of the physical fundamentals of the improved method involving the mapping of the tangential components of the electric and magnetic fields on the ice crystal surface to the far field on the basis of the electromagnetic equivalence theorem. By virtue of this mapping, the only approximation is in the calculation of the surface electric fields by means of the Fresnel coefficients and the applicable Snell's law based on the geometry. Phase interference and wave diffraction are both accounted for in the method.

The issue of absorption in the medium in the context of geometric ray tracing, referred to as the inhomogeneous effect, was subsequently discussed. We showed that the phase propagation of a wave inside the medium is determined by an adjusted real part of the refractive index through the Fresnel and Snell laws, whereas attenuation of the wave amplitude is determined by an adjusted imaginary part of the refractive index. The adjusted refractive indices are derived on the basis of the fundamental electromagnetic wave theory. We further described an efficient way of performing geometric ray tracing in complex-shaped ice particles via the Monte Carlo method and presented a methodology to treat the possibility of irregularity of the ice crystal surface using the stochastic approach. Comparisons

of the phase function results derived from the theory and laboratory-controlled experiments were also made.

For size parameters smaller than about 20, we adopted a finite difference time domain technique for light scattering by small nonspherical ice crystals, which solves the Maxwell equations by finite difference numerical means in the time domain by discretizing the scatterer with given optical properties. The solution requires the imposition of a numerically stable absorbing boundary condition. The frequency spectrum of the time-dependent results can be obtained by using a suitable Gaussian pulse via the discrete Fourier transform technique. The far-field solution can be derived by employing a surface or a volume integration approach. The method that we have developed was verified through comparisons with the exact Lorenz–Mie results for spheres and infinite circular cylinders and was shown to be efficient and accurate for size parameters on the order of 20. It can also be effectively applied to small inhomogeneous particles such as aerosols.

We then presented a number of examples demonstrating the application of the unified theory for light scattering by ice crystals to remote sensing of ice crystal clouds and to investigation of the climatic effect of cirrus. We showed that interpretations of the bidirectional reflectance and polarization patterns measured from aircraft and satellites require the correct scattering, absorption, and polarization data for nonspherical ice crystals. Lidar backscattering observations of cirrus and contrail, particularly those utilizing the depolarization technique, also require the correct scattering information on nonspherical ice particles. Based on observations and appropriate ice cloud models, the ice crystal size and shape and optical depth information for cirrus can be inferred from the reflected solar intensity and polarization. Moreover, we illustrated that rich information on cirrus cloud composition and structure is contained in the 1.38-μm solar line spectra. Indeed, determination of the optical and microphysical properties of cirrus, subvisual cirrus, and contrails based on remote sensing presents a great challenge in view of the substantial variability of ice crystal sizes and shapes in space and time.

Finally, we discussed the importance of the scattering and absorption properties of nonspherical ice particles in conjunction with studies of cloud radiative forcing and climatic temperature perturbations resulting from uncertainties in the cirrus cloud parameters. We used the models of ice columns/plates and equivalent spheres to illustrate the effect of nonspherical shapes on the broad-band solar albedo and showed that cloud albedo is much smaller for equivalent spheres because of stronger forward scattering. Although the temperature responses to climate change are complex and involve numerous dynamic and thermodynamic factors and feedbacks, we illustrate that the physically based single-scattering properties of nonspherical ice crystals are relevant and significant in the modeling of cirrus cloud radiative transfer for climate studies.

ACKNOWLEDGMENTS

Support of this research work includes National Science Foundation Grant ATM-97-96277, NASA Grants NAG-5-6160 and NAG-1-1966, and DOE Grant DE-FG03-95ER61991.